Effect of Compositional Fluctuations on the Phase Transitions in $(Nd_{1/2}Sr_{1/2})MnO_3$

P. M. Woodward,*,[†] D. E. Cox,[‡] T. Vogt,[‡] C. N. R. Rao,[§] and A. K. Cheetham[||]

Department of Chemistry, The Ohio State University, Columbus, Ohio 43210-1185; Physics Department, Brookhaven National Laboratory, Upton, New York 11973; Solid State and Structural Chemistry Unit, Indian Institute of Science, Bangalore 560012, India; and Materials Research Laboratory, University of California, Santa Barbara, California 93106

Received May 11, 1999. Revised Manuscript Received September 9, 1999

High-resolution synchrotron X-ray and neutron powder diffraction techniques have been used to investigate the structural and magnetic phase transitions in two polycrystalline samples with nominal composition $(Nd_{0.5}Sr_{0.5})MnO_3$. The first sample separates into three coexisting macroscopic phases at low temperature: a ferromagnetic (FM) phase, an orbitally ordered antiferromagnetic A-type (AFM-A) phase, and the majority phase, which shows charge, orbital, and antiferromagnetic CE-type (AFM-CE) ordering. The second sample shows a clean transition from the FM state into the AFM-CE state. The unusual behavior of the first sample is associated with a slight excess of Mn^{4+} and a wider compositional range with respect to the second sample and illustrates the very delicate competition between these three states near a Mn^{4+}:Mn^{3+} ratio of unity, where both electron delocalization and charge-ordering are known to occur. The charge-ordered structure of $Nd_{0.5}Sr_{0.5}MnO_3$ is reported.

Introduction

The current interest in the manganate perovskites, $Ln_{1-x}A_xMnO_3$, where A is a divalent alkaline earth ion and Ln is a trivalent lanthanide cation, has been stimulated largely by the colossal magnetoresistive (CMR) behavior displayed by many of these compounds.[1] There is widespread agreement that in the $Ln_{1-x}A_xMnO_3$ system, double-exchange[2] is largely responsible for the strong correlation between magnetic and transport properties.[3] The octahedral coordination of oxygen about manganese splits the Md 3d orbitals into t_{2g} and e_g states.[4] Strong Hund's rule coupling dictates localized electron configurations of $t_{2g}{}^3e_g{}^1$ for Mn^{3+} and $t_{2g}{}^3e_g{}^0$ for Mn^{4+}. Double-exchange allows electron transfer between neighboring Mn^{3+} and Mn^{4+} ions, thereby delocalizing the e_g electrons, as long as the spins of the d electrons are aligned parallel or nearly parallel. Therefore, theoretical models of these materials based solely on the double-exchange interaction predict a phase transition from a poorly conducting paramagnetic (PM) state to a metallic ferromagnetic (FM) state as the temperature is lowered. Such behavior is qualitatively observed for samples with doping levels in the approximate range, $0.4 \geq x \geq 0.2$. However, recent theories have shown that strong electron−phonon coupling, originating from the Jahn−Teller distortion of the octahedral environment about the Mn^{3+} ion, must also be considered to explain the behavior of these materials.[5]

The importance of electron−phonon coupling is clearly evident for compositions with $x \geq 0.4$ where charge, orbital, and antiferromagnetic (AFM) ordering compete with the FM metallic state. This competition can lead to a complex series of phase transitions, including the intriguing possibility that electron localization can drive a material, which is homogeneous when the electrons are itinerant, to phase separate, by inhomogeneously redistributing the electron density. Such behavior is observed, on the nanoscale, as stripe formation in the cuprates,[6] nickelates,[7] and manganates.[8] Charge ordering in the manganates[9,10] can be thought of as a similar phenomenon in that the conduction electrons, which are

---

* Corresponding author. E-mail: woodward@chemistry.ohio-state.edu.

[†] The Ohio State University.

[‡] Brookhaven National Laboratory.

[§] Indian Institute of Science.

[||] University of California-Santa Barbara.

(1) Jin, S.; McCormack, M.; Tiefel, T. H.; Ramesh, R. *J. Appl. Phys.* **1994**, *76*, 6929.

(2) Zener, C. *Phys. Rev.* **1951**, *82*, 403. Anderson, P. W.; Hasegawa, H. *Phys. Rev.* **1955**, 100, 675. deGennes, P.-G. *Phys. Rev.* **1960**, *118*, 141.

(3) Goodenough, J. B. *Phys. Rev.* **1955**, *100*, 564.

(4) The symmetry classifications t_{2g} and e_g strictly apply only to pure octahedral coordination about Mn as found in the ideal cubic perovskite structure. Compounds in the $Ln_{1-x}A_xMnO_3$ system are always found to be distorted from cubic symmetry, but since the symmetry is still pseudo-cubic t_{2g} and e_g remain useful, although not strictly valid, descriptors.

(5) Millis, A. J.; Shraiman, B. I.; Mueller, R. *Phys. Rev. Lett.* **1996**, *77*, 175. Röder, H.; Zhang J.; Bishop, A. R. *Phys. Rev. Lett.* **1996**, *76*, 1356.

(6) Emery, V. J.; Kivelson, S. A.; Lin, H. Q. *Phys. Rev. Lett.* **1990**, *64*, 475. Dagotto, E. *Rev. Mod. Phys.* **1994**, *66*, 763. Tranquada, J. M.; Sternlieb, B. J.; Axe, J. D.; Nakamura, Y.; Uchida, S. *Nature* (London) **1995**, *375*, 561. Haas, S.; Dagotto, E.; Nazarenko, A.; Rierra, J. *Phys. Rev. B* **1995**, *51*, 5989. Löw, U.; Emery, V. J.; Fabricius, K.; Kivelson, S. A. *Phys. Rev. Lett.* **1994**, *72*, 1918.

(7) Tranquada, J. M.; Wochner, P.; Buttrey, D. J. *Phys. Rev. Lett.* **1997**, *79*, 2133.

(8) Chen, C. H.; Cheong, S.-W.; Hwang, H. Y. *J. Appl. Phys.* **1997**, *81*, 4326. Mori, S.; Chen, C. H.; Cheong, S.-W. *Nature (London)* **1998**, *392*, 473.

(9) Radaelli, P. G.; Cox, D. E.; Marezio, M.; Cheong, S.-W. *Phys. Rev. B* **1997**, 55, 3015.

(10) Rao, C. N. R.; Arulraj, A.; Santhosh, P. N.; Cheetham, A. K. *Chem. Mater.* **1998**, *10*, 2714.

10.1021/cm990281d CCC: $18.00

homogeneously distributed in the metallic state, preferentially localize onto the Mn^{3+} sites and depopulate the Mn^{4+} sites. Thus on the length scale of the unit cell such a distribution of charge is inhomogeneous.

There have recently been a number of theoretical predictions[11,12] and a growing body of experimental evidence for phase separation in manganate systems.[13] In most cases, this separation involves the formation of clusters or droplets of one phase within another. This behavior has been seen in $La_{1-x}Sr_xMnO_3$, $La_{1-x}Ca_xMnO_3$, and $Pr_{1-x}Ca_xMnO_3$ in or close to the ferromagnetic metallic (FMM) region of the phase diagram. The coexistence of ferromagnetic clusters and another phase (which may be antiferromagnetic (AF) and/or charge-ordered (CO)) has been revealed by a variety of experimental techniques. A related but quite distinct phenomenon is macroscopic phase separation. The term macroscopic is used to stress the fact that each phase has distinct domains with dimensions on the order of 1000 Å or more, as demonstrated by the presence of sharp Bragg peaks in the powder diffraction pattern. This is quite different from the nanoscale phase separation associated with stripe formation, which actually describes the inhomogeneous distribution of charge and/or spin over a length scale of tens of angstroms, within a material which is single phase on a macroscopic length scale. However, as emphasized by Yunoki et al.,[12] Coulomb forces will surely prevent the macroscopic accumulation of charge within a phase-separated regime without some mechanism for charge compensation such as high ionic mobility. An example of this type is the macroscopic phase separation observed in systems such as $La_2MO_{4+\delta}$ (M = Cu, Ni), in which the excess interstitial oxygen has high mobility close to room temperature.[14] Structural considerations render this mechanism highly unlikely in the stoichiometric perovskite structure. Nonetheless, there is a growing body of evidence from powder diffraction data that macroscopic phase separation does occur in the manganates, as shown by the appearance and coexistence of two different crystallographic phases over a wide range of temperature in a material which exhibits an apparently single-phase diffraction pattern at room temperature; e.g. $Pr_{0.6}Sr_{0.4}MnO_3$,[15] $Pr_{0.5}Sr_{0.5}MnO_3$,[16] $Nd_{0.25}La_{0.25}Ca_{0.5}MnO_3$,[17] and $La_{0.53}Ca_{0.47}MnO_3$.[18] There are also several reports of the coexistence of two magnetic states over a wide temperature range, as shown by the appearance of two sets of magnetic peaks in the neutron diffraction patterns. In the present work, high-resolution synchrotron X-ray and neutron powder diffraction techniques have been used to study the crystallographic and magnetic structures of two polycrystalline samples of nominal composition $Nd_{0.5}Sr_{0.5}MnO_3$ over the temperature range 15−300 K. We have observed that although both samples give sharp and symmetric X-ray peaks at 300 K indicative of homogeneous, single-phase material, as the temperature is lowered the first sample separates into first two and then three coexisting macroscopically distinct phases. Each phase is characterized by different lattice parameters and magnetic structures. In contrast, the second material is single-phase over most of the temperature range except for a narrow region in the vicinity of the charge-ordering transition at ~150 K. We speculate that the different sequences of phase transitions observed in these two samples can be attributed to differences in their compositional homogeneity. A preliminary account of this work has been given in ref 19.

Previous Studies

Previous work on $Nd_{0.5}Sr_{0.5}MnO_3$ has shown it to undergo a series of phase transitions as a function of temperature, going from a PM metal at room temperature,[20,21] to a FM metal below 250 K, and finally to a charge-ordered AFM insulating state below 158 K.[20,22] The charge-ordered state in $Nd_{0.5}Sr_{0.5}MnO_3$ is rather fragile. Application of a magnetic field stabilizes the FM state at temperatures far below the charge-ordering temperature, T_{CO}.[20] A small change in the doping level, to a stoichiometry of $Nd_{0.45}Sr_{0.55}MnO_3$, is enough to destroy the charge-ordered state and change the AFM structure from CE-type to A-type.[22] Increasing the mean radius of the Ln/A cations, $\langle r_A \rangle$, by substituting lanthanum for neodymium, ($Nd_{0.5-x}La_xSr_{0.5}$)MnO_3, destroys the AFM-CE state, stabilizing the FM state down to at least 5 K when $x \geq 0.6$.[23] Reducing $\langle r_A \rangle$ by substituting samarium for neodymium, ($Nd_{0.5-x}Sm_xSr_{0.5}$)MnO_3, lowers T_{CO} to the point where a supercooled, metastable FM state is obtained at low temperatures.[24,25]

$Nd_{0.5}Sr_{0.5}MnO_3$ has an orthorhombic perovskite-like structure, but there is a lack of agreement about the proper space group symmetry. Caignaert et al.[21] reported the symmetry as *Imma*, which corresponds to a rather rare type of distortion from the ideal cubic perovskite structure caused by tilting of the octahedra about [101] (Glazer tilt system $a^-b^0a^-$).[26] On the other hand, Moritomo et al.[23] determined the symmetry as *Pnma*,[27] which is much more common in perovskites and corresponds to tilting about [101] and [010] (tilt system $a^-b^+a^-$), and this symmetry has been assumed in

---

[11] Furakawa, N. *J. Phys. Soc. Jpn.* **1994**, *63*, 3214. Riera, J.; Hallberg, K.; Dagotto, E. *Phys. Rev. Lett.* **1997**, *79*, 713.

[12] Yunoki, S.; Hu, J.; Malvezzi, A. L.; Moreo, A.; Furukawa, N.; Dagotto, E. *Phys. Rev. Lett.* **1998**, *80*, 845.

[13] Moreo, A.; Yunoki, S.; Dagotto, E. *Science* **1999**, *283*, 2034.

[14] Rice, D. E.; Buttrey, D. J. *J. Solid State Chem.* **1993**, *105*, 197. Radaelli, P. G.; Jorgensen, J. D.; Kleb, R.; Hunter, B. A.; Chou, F. C.; Johnston, D. C. *Phys. Rev. B* **1994**, *49*, 6239.

[15] Ritter, C.; Radaelli, P. G.; Lees, M. R.; Barratt, J.; Balakrishnan, G.; McK. Paul, D. K. *J. Solid State Chem.* **1996**, *127*, 276.

[16] Damay, F.; Martin, C.; Hervieu, M.; Maignan, A.; Raveau, B.; Andre, G.; Bouree, F. *J. Magn. Magn. Mater.* **1998**, *184*, 71.

[17] Arulraj, A.; Biswas, A.; Raychaudhuri, A. K.; Rao, C. N. R.; Woodward, P. M.; Vogt, T.; Cox, D. E.; Cheetham, A. K. *Phys. Rev. B* **1998**, *57*, R8115.

[18] Rhyne, J. J.; Kaiser, H.; Luo, H.; Xiao, G.; Gardel, M. L. *J. Appl. Phys.* **1998**, *83*, 7339.

[19] Woodward, P. M.; Cox, D. E.; Vogt, T. *J. Superconductivity*, in press.

[20] Kuwahara, H.; Tomioka, Y.; Asamitsu, A.; Moritomo, Y.; Tokura, Y. *Science* **1995**, *270*, 961.

[21] Caignaert, V.; Millange, F.; Hervieu, M.; Suard, E.; Raveau, B. *Solid State Commun.* **1996**, *99*, 173.

[22] Kawano, H.; Kajimoto, R.; Yoshizawa, H.; Tomioka, Y.; Kuwahara, H.; Tokura, Y. *Phys. Rev. Lett.* **1997**, *78*, 4253.

[23] Moritomo, Y.; Kuwahara, H.; Tomioka, Y.; Tokura, Y. *Phys. Rev. B* **1997**, *55*, 7549.

[24] Tokura, Y.; Kuwahara, H.; Moritomo, Y.; Tomioka, Y.; Asamitsu, A. *Phys. Rev. Lett.* **1996**, *76*, 3184.

[25] Kuwahara, H.; Moritomo, Y.; Tomioka, Y.; Asamitsu, A.; M. Kasai, R. Kumai, Tokura, Y. *Phys. Rev. B*, **1997**, *56*, 9386.

[26] Glazer, A. M. *Acta Crystallogr.* **1972**, *B28*, 3385.

[27] These authors used the *Pbnm* setting, but here and elsewhere in this paper we will use the conventional *Pnma* setting, which is obtained from *Pbnm* by a change of axes from *abc* to *bca*.

several subsequent papers.[22,25,28,29] With *Imma* symmetry, the Mn−O−Mn angles in the *ac* plane are closer to 180° than the Mn−O−Mn angles in the *b* direction.[30] This bond-angle anisotropy increases the spatial overlap of Mn e_g and O 2pσ orbitals, and hence the one-electron bandwidth (W), in the *ac* plane. Thus the anisotropic distribution of Mn−O−Mn bond angles inherent to the $a^-b^0a^-$ tilt system should favor the AFM-A type structure,[22] which contains FM coupling in the *ac* plane, and AFM coupling in the *b* direction.

In the $Nd_{1-x}Sr_xMnO_3$ system, the fact that three different ground states (FM, AFM-CE, and AFM-A) are observed over a rather narrow compositional range, $0.45 < x < 0.55$, suggests that the energies of these three states are quite similar. It is well-known that the e_g electrons are delocalized in the FM state. Furthermore, it has been shown that the e_g electrons are also delocalized in the AFM-A state when $x > 0.5$.[28,29,31] In the FM state, the delocalization occurs isotropically, whereas in the AFM-A state overlap of the $3d_{x^2-z^2}$ orbitals on manganese with the O 2pσ orbitals leads to a pseudo-2D band, and delocalization of the e_g electrons in the *ac* plane.[28] In contrast, the charge-ordered distribution of Mn^{3+}/Mn^{4+} found in the AFM-CE state can occur only in the presence of localized e_g electrons. The Coulomb energy which accompanies formation of an ordered Mn^{3+}/Mn^{4+} distribution is essential in stabilizing the AFM-CE state over the competing states (FM and AFM-A). As evidence of this competition, consider the fact that $T_N = T_{CO}$ in $Nd_{0.5}Sr_{0.5}MnO_3$, implying that both antiferromagnetic superexchange and Coulomb contributions are necessary to stabilize the AFM-CE state.[32] The importance of the Coulomb stabilization energy, which will be maximized at $x = 0.5$, is further demonstrated by the narrow compositional range over which the AFM-CE state is observed.[29]

This is in contrast to the behavior of many $Ln_{1-x}Ca_xMnO_3$ compositions,[33,34] where the electrons have a stronger tendency to localize (due to increased bending of the Mn−O−Mn bonds), and consequently show charge ordering over a fairly wide range of *x*.

Experimental Section

Two samples were prepared using conventional solid-state synthesis techniques. Sample 1 was prepared from a stoichiometric mixture of Nd_2O_3, $SrCO_3$, and Mn_3O_4. After an initial prefiring to decompose the carbonate, sample 1 was pelletized and heated gradually (5 °C/min) to 1400 °C and kept there for 12 h. The temperature was then increased to 1500 °C (5 °C/min) and maintained there for an additional 12 h. Finally, the pellet was cooled at 5 °C/min to room temperature. The second sample (sample 2) was prepared in a similar manner, from Nd_2O_3, $SrCO_3$, and MnO. Initial annealing cycles were carried out in air in the 1000−1200 °C range, followed by grinding and pelletization. The sample was then heated to 1500 °C for ∼12 h and then furnace-cooled over a period of 2−4 h.

X-ray powder diffraction data were collected on beamline X7A at Brookhaven's National Synchrotron Light Source. High-resolution variable-temperature measurements were taken by mounting a portion of the sample onto a flat-plate Cu sample holder and loading it into a closed-cycle helium cryostat in symmetric reflection geometry. To obtain optimal resolution a double-crystal Si(111) monochromator was used in the incident beam, and a flat Ge(220) analyzer crystal in the diffracted beam. The wavelength was determined by calibration with a reference sample of highly crystalline Si for which sample broadening effects are negligible. Two wavelengths were employed during the course of this study, 1.19985 and 0.79935 Å. We note that in this configuration the instrumental resolution (fwhm on the 2θ scale at $\lambda = 1.2$ Å) is ∼0.01° in the low-angle region out to $2\theta \cong 45°$ ($\Delta d/d = 2-3 \times 10^{-4}$), an order-of-magnitude better than that of laboratory diffraction equipment typically used for the characterization of ceramic samples, and also that of most neutron powder diffractometers. Data were collected at several temperatures between 15 and 300 K by scanning in 0.005° intervals over selected angular regions while the sample was rocked over a few degrees to improve powder averaging.

Additional X-ray data were collected at a wavelength of 0.79001 Å with a linear position-sensitive detector (PSD) mounted on the scattering arm in place of the crystal-analyzer. The linear PSD is a proportional multiwire device of the type described by Smith[35] filled with a 90%:10% Kr/CO_2 mixture at a pressure of 4 bar and operating in the escape-peak mode. For these measurements, the sample was loaded into a 0.2-mm-diameter thin-walled glass capillary and mounted in a closed-cycle He cryostat. In this configuration, the instrumental resolution is somewhat lower (∼0.03°) but the counting rates are much faster than they are with the crystal-analyzer geometry, enabling extended scans to be made with good counting statistics in a few hours. Furthermore, the use of capillary geometry and larger rocking angles greatly reduces systematic errors due to preferred orientation and inadequate powder averaging. Consequently, the data sets generally yield Rietveld fits of excellent quality. Finally, neutron data were collected on sample 1 at NIST from the same sample at several temperatures between 15 and 300 K using the 32-detector powder diffractometer BT1 at a wavelength of 2.077 Å, with in-pile collimation of 7′. Structural refinements were performed using the Rietveld method as implemented in the GSAS software suite.[36]

Results

Compositional Analysis. Both samples 1 and 2 were made from stoichiometric ratios of the respective oxides and carbonates. Therefore, they are expected to have a stoichiometric ratio of neodymium, strontium, and manganese.[37] Nonetheless, in light of the unusual phase transition behavior exhibited by the first sample we performed a combined Rietveld refinement using both neutron and X-ray data in an attempt to determine the metal stoichiometry. The results are shown in Table 1 for three different refinement models: one with A-site vacancies, $(Sr_{0.5}Nd_{0.5})_{1-y}MnO_{3-x}$ (model I), one with no cation vacancies but with a variable Nd:Sr ratio, $(Sr_{0.5+y}Nd_{0.5-y})MnO_{3-x}$ (model II), and one where the ideal cation stoichiometries are maintained (model III). The refinement results are somewhat inconclusive. The

---

(28) Akimoto, T.; Maruyama, Y.; Moritomo, Y; Nakamura, A.; Hirota, K.; Ohoyama, K.; Ohashi, M. *Phys. Rev. B* **1998**, *57*, R5594.

(29) Moritomo, Y.; Akimoto, T.; Nakamura, A.; Ohoyama, K.; Ohashi, M. *Phys. Rev. B* **1998**, *58*, 5544.

(30) Woodward, P. M.; Vogt, T.; Cox, D. E.; Arulraj, A.; Rao, C. N. R.; Karen, P.; Cheetham, A. K. *Chem. Mater.* **1998**, *10*, 3652.

(31) Yoshizawa, H.; Kawano, H.; Fernandez-Baca, J. A.; Kuwahara, H.; Tokura, Y. *Phys. Rev. B* **1998**, *58*, R571.

(32) Kumar, N.; Rao, C. N. R. *J. Solid State Chem.* **1997**, *129*, 363.

(33) Wollan, E. O.; Koehler, W. C. *Phys. Rev.* **1955**, *100*, 545. Schiffer, P.; Ramirez, A. P.; Bao, W.; Cheong, S.-W. *Phys. Rev. Lett.* **1995**, *75*, 3336.

(34) Jirak, Z.; Krupicka, S.; Simsa, Z.; Dlouha, M.; Vratislav, S. *J. Magn. Magn. Mater.* **1985**, *53*, 153.

(35) Smith, G. C. *Synchrotron Rad. News* **1991**, *4*, no. 3, 24.

(36) Larson, A. C.; Von Dreele, R. B. *GSAS Software Suite*; LANSCE-Los Alamos National Laboratory: Los Alamos, NM.

(37) It is well-known that the oxygen content in the manganates is sensitive to the annealing conditions.

Table 1. Compositional Analysis for Sample 1

model	R_{wp}, %	y^a	x^b	Mn valence
$(Sr_{0.5}Nd_{0.5})_{1-y}MnO_{3-x}$	9.40	0.026(1)	0.012(1)	3.541
$(Sr_{0.5+y}Nd_{0.5-y})MnO_{3-x}$	9.41	0.046(3)	0.010(1)	3.526
$(Sr_{0.5}Nd_{0.5})MnO_{3-x}$	9.48	0	0.001(1)	3.498

[a] The value of y was determined from combined refinements of the X-ray and neutron diffraction patterns. [b] The value of x was determined from iodometric titrations

Table 2. Lattice Parameters and Unit Cell Volumes as Determined at Room Temperature Using the Crystal Analyzer Detector[a]

	sample 1		sample 2
wavelength, Å	1.19985	0.79935	0.79935
a (Å)	5.4294(3)	5.4299(3)	5.4312(3)
b (Å)	7.6291(4)	7.6296(5)	7.6321(4)
c (Å)	5.4737(3)	5.4736(3)	5.4754(3)
volume (Å^3)	226.73(2)	226.76(2)	226.96(2)

[a] The values were obtained from a least-squares fit to the first 11 peaks with the zero offset included as a variable parameter. The correct space group is *Imma*.

first two models give almost identical fits to the diffraction patterns, and the quality of fit does not degrade significantly for model III.

The oxygen content of both samples was determined iodometrically as described in ref 30. Proper interpretation of the titration results requires knowledge of the proper cation stoichiometry. Table 1 gives the stoichiometry of sample 1 (using a combination of the refinement and titration results) corresponding to each of the three models discussed above. Although these experiments do not conclusively determine the stoichiometry of sample 1, the data are consistent with a Mn^{4+}:Mn^{3+} ratio slightly in excess of unity, in which case model I is to be preferred, since a slight deficiency in the Nd/Sr content can be plausibly attributed to a small excess of Mn in nominally stoichiometric Mn_3O_4, while the Sr excess implied by model II is well outside possible experimental error. Furthermore, the stoichiometry as suggested by model II would be inconsistent with the published lattice parameter data described in the next section.

Refinements suggest that sample 2 has the expected stoichiometric ratio of metals. Iodometric analysis of the second sample showed a very slight excess of Mn^{3+} corresponding to the overall composition $(Nd_{0.5}Sr_{0.5})MnO_{3-x}$ with $x = 0.003(1)$.[38] Thus, we conclude that sample 2 is very close to the ideal stoichiometry. As discussed later, the observation that the unit cell volume of sample 1 is smaller than that of sample 2 also is a strong indication that the Mn^{4+}:Mn^{3+} ratio in sample 1 is slightly in excess of unity.

Sample 1—Diffraction Results. The high-resolution X-ray pattern collected at 300 K showed a single orthorhombic phase with sharp and symmetric Bragg peaks and lattice parameters $a = 5.4294(3)$, $b = 7.6291(4)$, and $c = 5.4737(3)$ Å (Table 2). All of the observed peaks satisfied the reflection conditions hkl: $h + k + l = 2n$; and $hk0$: $h = 2n$, consistent with *Imma* symmetry as reported by Caignaert et al.[21] A careful check was made for additional peaks such as (111) and (210) which are characteristic of *Pnma* symmetry and would violate the body-centering condition, but no evidence was found for such peaks. The lattice parameters are in good agreement with previously reported results.[20−22] Additional information about the microstructure was obtained from a Williamson−Hall plot,[39] which relates the measured peak widths to the mean crystallite size, L, and the distribution (fwhm) in d spacing, $\Delta d/d$, for different classes of reflections through the expression:

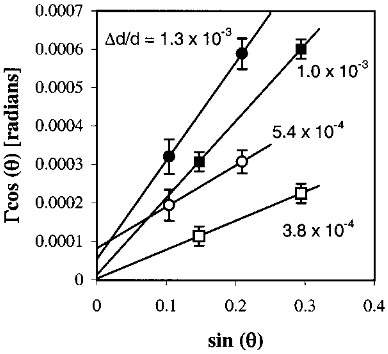

Figure 1. Williamson−Hall plot constructed using fwhm's and peak positions obtained from the X-ray diffraction data collected using the crystal analyzer detector. The filled symbols correspond to sample 1, while the open symbols correspond to sample 2. The circles represent (020) and (040) reflections. The squares represent (121) and (242) reflections. The fwhm's were corrected for instrumental resolution. The extracted $\Delta d/d$values are listed in the figure.

$$\Gamma\cos(\theta) = (K\lambda/L) + 2(\Delta d/d)\sin(\theta)$$

where K is a shape factor close to unity, Γ is the fwhm, and λ is the wavelength of the radiation. From such a plot (see Figure 1) of the peak widths of selected pairs of reflections, corrected for instrumental resolution, we estimate the average crystallite size, L, to be in the region of a micrometer for both samples. Furthermore, we interpret $\Delta d/d$ as reflecting a distribution of lattice parameters corresponding to compositional fluctuations in the Nd:Sr ratio. On the basis of the variation of the lattice parameters of $Nd_{1-x}Sr_xMnO_3$, for x between 0.5 and 0.54,[29] we estimate the long-range compositional fluctuations in the Nd:Sr ratio to be within ±0.01 for sample 1, and ±0.005 for sample 2. Thus by diffraction standards far more stringent than typically quoted, we would conclude that both samples are single phase and homogeneous. In particular, we note that there is no evidence of any asymmetric broadening or shoulders indicative of two very similar coexisting phases, as, for example, observed in analogous synchrotron X-ray studies of layered manganates of the type $La_{2-x}Sr_{1+x}Mn_2O_7$.[40,41]

On cooling the sample, a number of striking and unexpected changes were observed as illustrated in Figure 2, which shows the pseudo-cubic perovskite (110) reflection at three different temperatures. At room temperature and down to 225 K, this reflection is split

---

[38] Three trials of the iodometric titration were carried out. The error of 0.001 in the oxygen content represents the standard deviation of these three trials.

[39] Williamson, G. K.; Hall, W. H. *Acta Metall.* **1953**, *1*, 22.

[40] Battle, P. D.; Cox, D. E.; Green, M. A.; Milburn, J. E.; Spring, L. E.; Radaelli, P. G.; Rosseinsky, M. J.; Vente, J. F. *Chem. Mater.* **1997**, *9*, 1042.

[41] Argyriou, D. N.; Mitchell, J. F.; Radaelli, P. G.; Bordallo, H. N.; Cox, D. E.; Medarde, M.; Jorgensen, J. D. *Phys. Rev. B* **1999**, *59*, 8695.

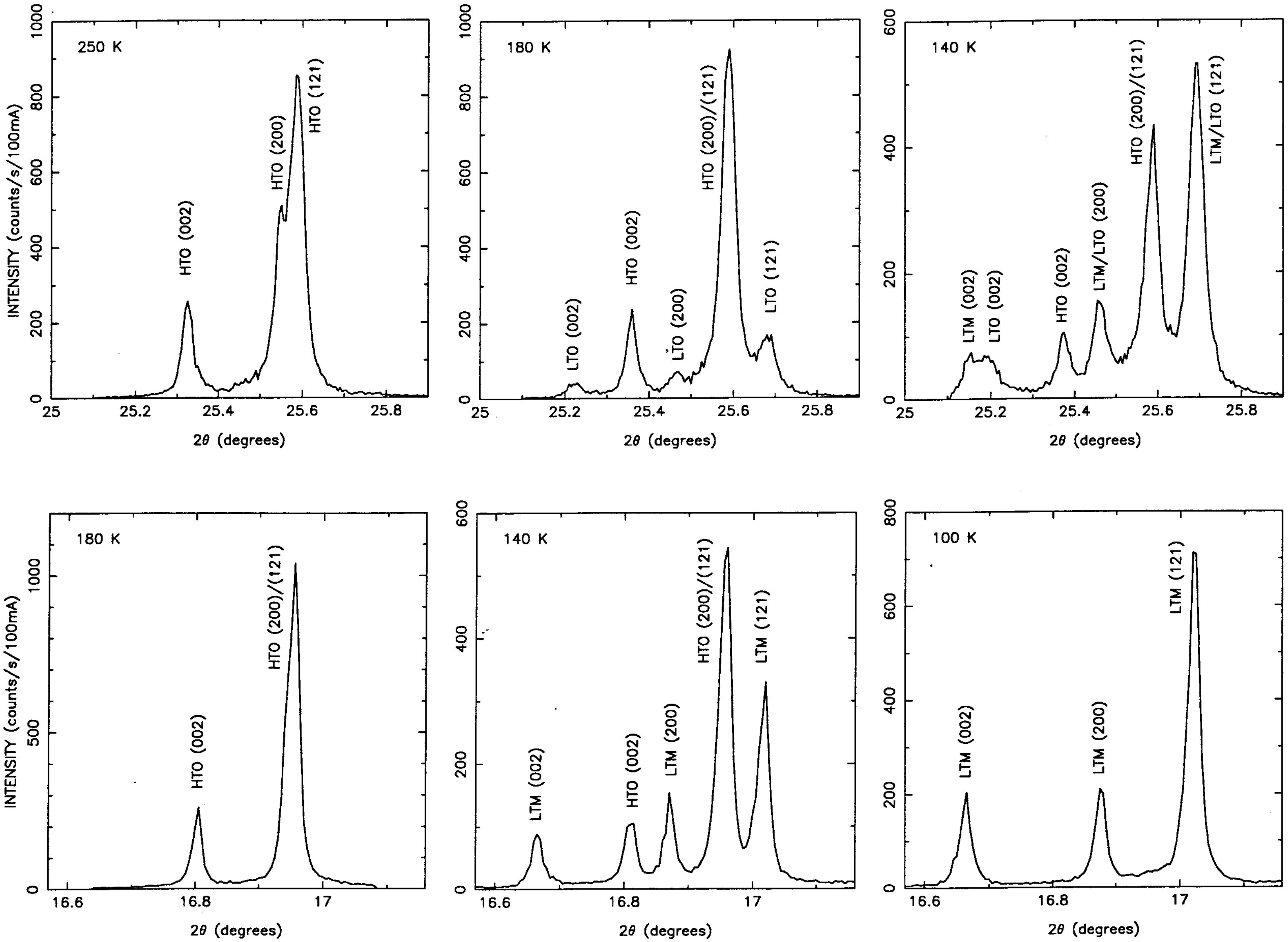

Figure 2. Splitting of the pseudocubic (110) reflection in the high-resolution synchrotron X-ray data collected from (a) sample 1 at 250, 180, and 140 K (top panel, $\lambda = 1.1999$ Å) and (b) sample 2 at 180, 140, and 100 K (bottom panel, $\lambda = 0.79935$ Å). Peaks are labeled with their phase and orthorhombic peak indices.

into three sharp and distinct peaks as a consequence of the octahedral tilting distortion, which leads to orthorhombic symmetry (the HTO phase). Below 225 K, a second set of three peaks is seen, well-resolved from those of the HTO phase. Rietveld refinements, to be described later, confirm that these peaks belong to a second orthorhombic phase (LTO), also of the perovskite type with *Imma* symmetry. Finally, below 150 K peaks associated with a third phase (LTM) appear. Although these peaks overlap closely those of the LTO phase, reflections having a significant *l* component (such as the (002) peaks in Figure 2) are clearly resolved. Structure refinements confirm that these peaks belong to a distinct phase, which is metrically orthorhombic, but has monoclinic $P2_1/m$ symmetry.[9] These three phases coexist down to the lowest temperature attained (15 K). Multiple warming and cooling cycles show the phase transition behavior to be reversible. Furthermore, these transitions are not accompanied by any significant broadening of the peaks associated with the development of internal strain or the breakdown of the crystallites into small domains. Thus it appears that the macroscopic dimensions of the individual crystallites are largely preserved. This behavior is strikingly different from that of $La_{0.5}Ca_{0.5}MnO_3$, which undergoes a transition from FM to AFM-CE type characterized by very pronounced and complex peak broadening effects in the transition region.[9]

The corresponding neutron data (Figure 3) show the onset of ferromagnetic order in the HTO phase between 250 and 225 K as revealed by the large increase in the intensity of the (200) reflection, in agreement with previous studies.[20,22] At 200 K, additional peaks are seen, consistent with the antiferromagnetic A-type structure previously reported for $Nd_{0.45}Sr_{0.55}MnO_3$ below 225 K[22] and for $Nd_{0.48}Sr_{0.52}MnO_3$ below 200 K.[29] Finally, below 150 K, yet another set of peaks appears corresponding to the antiferromagnetic CE-type structure observed for $Nd_{0.5}Sr_{0.5}MnO_3$ below 160 K.[22] The appearance of the AFM A-type and CE-type peaks coincides with the emergence of the LTO and LTM phases in the X-ray data, strongly suggesting that the three magnetic structures are associated with the three macroscopically distinct crystallographic phases. It should be noted that despite the fact that BT1 is a high-resolution neutron powder diffractometer, it was not possible to resolve nor even distinguish overlapping LTO and LTM peaks, nor would this be possible with a standard laboratory X-ray diffractometer.

At 300 K, structural refinements[36] using both the X-ray PSD and the neutron data gave very satisfactory fits to an orthorhombic structure with *Imma* symmetry. Structural refinements at lower temperatures confirm the appearance of the LTO phase below 225 K, which also has a perovskite-type structure with *Imma* symmetry, and the LTM phase below 150 K. Refinement results at 300 and 160 K are given in Tables 3 and 4. Table 6 contains the Mn−O distances and Mn−O−Mn bond angles, while Table 8 lists the refined values of the magnetic moment of the manganese ion. The refined magnetic moments for the FM (HTO) and AFM A-type (LTO) phases are in good agreement (slightly larger for the LTO phase) with values previously observed for $(Nd_{0.5}Sr_{0.5})MnO_3$ and $(Pr_{0.5}Sr_{0.5})MnO_3$.[22] However, the refined moments for the charge-ordered AFM CE-type phase are significantly smaller (by a factor of ~2) than values previously observed for $(Nd_{0.5}Sr_{0.5})MnO_3$[22] and

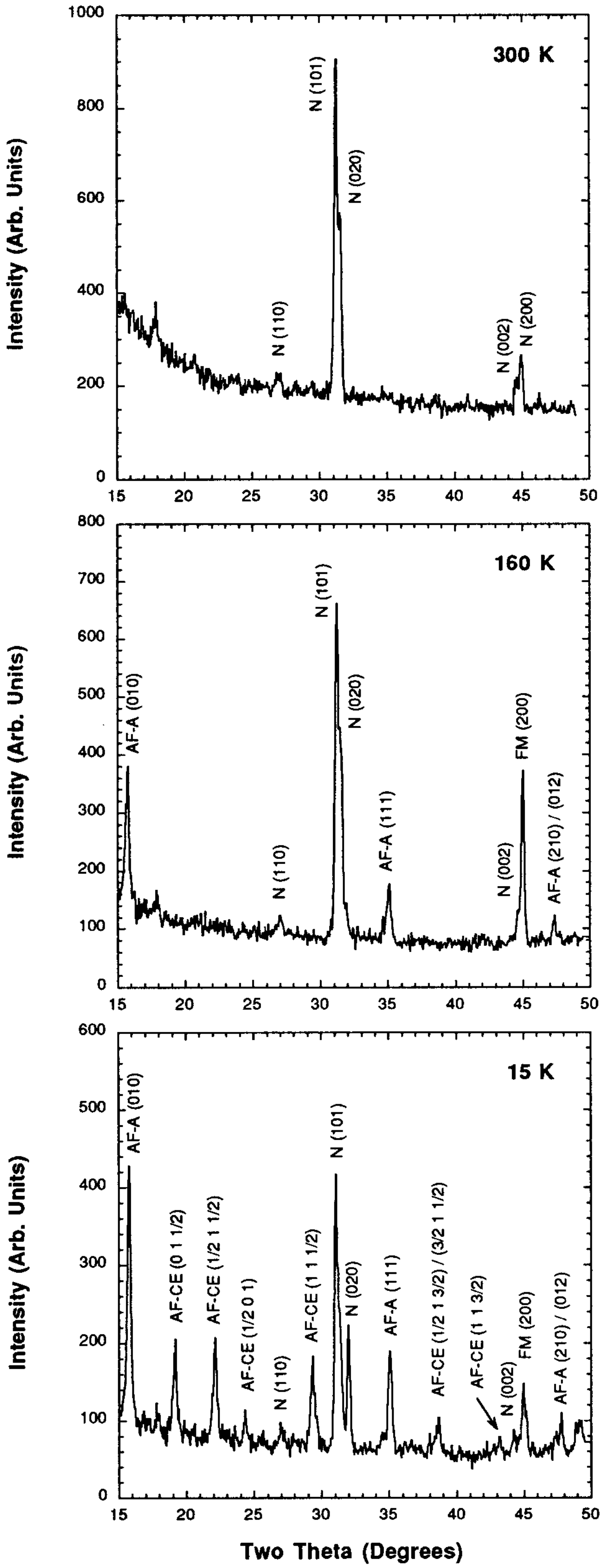

Figure 3. The low-angle region of the neutron diffraction data ($\lambda = 2.077$ Å) collected from sample 1 at 300, 160, and 15 K. Symbols represent nuclear (N), antiferromagnetic A-type (AF-A), antiferromagnetic CE-type (AFM-CE), and predominantly ferromagnetic (FM) reflections. Peak indices are given in parentheses.

Table 3. Refinement Statistics and Unit Cell Dimensions

	sample 1[a]			sample 2[a]		
	T = 300 K	T = 160 K		T = 300 K	T = 160 K	T = 50 K
R_{wp}, %	(X) 9.57 (N) 6.93	(X) 8.65 (N) 8.46		7.23	7.38	6.98
R_p, %	(X) 6.80 (N) 5.39	(X) 7.19 (N) 6.67		4.65	5.18	4.93
wavelength (Å)	(X) 2.077 (N) 0.7907	(X) 2.077 (N) 0.7907		0.80435	0.80435	0.80435
2θ range (deg)	(X) 8−62 (N) 20−145	(X) 11−36.5 (N) 10−145		10−82	10−62	10−71
phase	HTO	HTO	LTO	HTO	HTO	LTM
phase fraction, %	100	74	26	100	98[b]	95[c]
space group	*Imma*	*Imma*	*Imma*	*Imma*	*Imma*	$P2_1/m$
a (Å)	5.42977(3)	5.42143(6)	5.44677(7)	5.43153(3)	5.42204(3)	10.88967(5)
b (Å)	7.62999(3)	7.62948(8)	7.53398(9)	7.63347(4)	7.63081(4)	7.52496(3)
c (Å)	5.47349(2)	5.46660(5)	5.50025(8)	5.47596(3)	5.46821(3)	5.51502(3)
β (deg)	90	90	90	90	90	89.977(1)
volume (Å^3)	226.762(2)	226.113(4)	225.707(5)	227.041(2)	226.245(3)	451.924(4)

[a] Sample 1 results were obtained from combined refinements using both synchrotron X-ray and neutron powder diffraction data, whereas sample 2 results are based on synchrotron X-ray data only. [b] At 160 K sample 2 contained 2% of the LTM phase. [c] At 50 K sample 2 contained 5% of the HTO phase.

Table 4. Fractional Coordinates, Occupancies, and Displacement Parameters for Sample 1

atom	site	x	y	z	U_{iso}	valence[a]
			300 K (HTO)			
Nd/Sr	4e	0	0.25	−0.0018(2)	0.0064(1)	2.61
Mn	4b	0	0	0.5	0.0044(2)	3.75
O(eq)	8g	0.75	−0.0263(3)	0.25	*b*	2.10
O(ax)	4e	0	0.25	0.4455(6)	*c*	2.16
			160 K (HTO)			
Nd/Sr	4e	0	0.25	−0.0020(2)	0.0052(5)	2.66
Mn	4b	0	0	0.5	0.0001(9)	3.75
O(eq)	8g	0.75	−0.0267(4)	0.25	0.007(1)	2.12
O(ax)	4e	0	0.25	0.439(1)	0.018(2)	2.18
			160 K (LTO)			
Nd/Sr	4e	0	0.25	0.0007(8)	0.0052(5)	2.57
Mn	4b	0	0	0.5	0.0001(9)	3.83
O(eq)	8g	0.75	−0.0270(9)	0.25	0.007(1)	2.10
O(ax)	4e	0	0.25	0.464(3)	0.018(2)	2.20

[a] Bond valence sums were calculated using the program Valence.[44] [b] Anisotropic displacement parameters: U_{11} = 0.024(2), U_{22} = 0.024(2), U_{33} = 0.007(1), U_{13} = −0.012(1), U_{13} = U_{23} = 0. [c] Anisotropic displacement parameters: U_{11} = 0.014(3), U_{22} = 0.011(2), U_{33} = 0.024(3), U_{13} = U_{13} = U_{23} = 0.

Table 5. Fractional Coordinates, Occupancies, and Displacement Parameters for Sample 2

atom	site	x	y	z	U_{iso}	valence[a]
			300 K (HTO)			
Nd/Sr	4e	0	0.25	−0.0019(3)	0.0040(1)	2.58
Mn	4b	0	0	0.5	0.0015(2)	3.73
O(eq)	8 g	0.75	−0.0269(5)	0.25	0.0076(8)	2.09
O(ax)	4e	0	0.25	0.4462(9)	0.007(1)	2.14
			160 K (HTO)			
Nd/Sr	4e	0	0.25	−0.0021(2)	0.0019(1)	2.57
Mn	4b	0	0	0.5	0.0005(2)	3.77
O(eq)	8 g	0.75	−0.0240(7)	0.25	0.010(1)	2.10
O(ax)	4e	0	0.25	0.448(1)	0.001(1)	2.15
			50 K (LTM)			
Nd/Sr(1)	2e	0.25	0.25	0.0130(4)	0.0023(1)	2.63
Nd/Sr(2)	2e	0.75	0.25	−0.0130(4)	0.0023(1)	2.61
Nd/Sr(3)	2e	0.0	0.25	0.501(2)	0.0023(1)	2.67
Nd/Sr(4)	2e	0.5	0.25	0.499(2)	0.0023(1)	2.66
Mn(3A)	2a	0.0	0.0	0.0	0.0005(2)	3.49
Mn(3B)	2b	0.5	0.0	0.0	0.0005(2)	3.49
Mn(4)	4f	0.25	0.0	0.5166(8)	0.0005(2)	3.98
O(1)	4f	0.3732(8)	0.0292(5)	0.757(2)	0.007(1)	2.14
O(2)	4f	0.3733(8)	−0.0292(5)	0.277(2)	0.007(1)	2.05
O(3)	4f	0.1267(8)	0.0292(5)	0.757(2)	0.007(1)	2.14
O(4)	4f	0.1268(8)	−0.0292(5)	0.277(2)	0.007(1)	2.05
O(5)	2e	0.25	0.25	0.447(5)	0.002(1)	2.19
O(6)	2e	0.25	0.75	0.585(5)	0.002(1)	2.21
O(7)	2e	0.0	0.25	0.043(5)	0.002(1)	2.19
O(8)	2e	0.5	0.25	0.043(5)	0.002(1)	2.20

[a] Bond valence sums were calculated using the program Valence.[44]

$(La_{0.5}Ca_{0.5})MnO_3$.[9] The origin of this discrepancy is not clear, but may be a consequence of deviation from unity in the Nd:Sr ratio diminishing both the degree of Mn^{3+}:Mn^{4+} charge order and the CE-type magnetic order.

The evolution of the lattice parameters of the three phases is shown in Figure 4. At room temperature, the orthorhombic distortion is relatively small, consistent with the absence of orbital order resulting from the isotropic and delocalized nature of the e_g electrons. The smooth evolution of the lattice parameters of the HTO phase with temperature implies that no sudden carrier localization occurs as the temperature is reduced. In contrast, both the LTO and LTM phases show an abrupt expansion in the *ac* plane and contraction in the *b* direction, with respect to the HTO phase. This is the characteristic signature of a cooperative JT distortion, which is a consequence of preferential occupation of the e_g orbital in the *ac* plane (orbital ordering).[30,34] Therefore, we conclude that orbital ordering is present in the LTO and LTM phases, but not in the HTO phase.

It is difficult to unambiguously confirm charge ordering from the neutron data alone, due to the superposition of magnetic and nuclear scattering contributions. However, the occurrence of weak superlattice reflections in the X-ray data, consistent with the AFM-CE structure, is an unambiguous confirmation of charge ordering.[9] The strongest superlattice reflections are expected to be ($^1/_2$,2,3) and ($^3/_2$,2,3). Careful scans of the corresponding region of the X-ray diffraction patterns were made at selected temperatures, two of which are shown in Figure 5. At 160 K neither these nor any other superstructure reflections were seen, indicating that the LTO (AFM-A) phase is not charge-ordered. Weak superstructure reflections are visible at 140 K, which grow stronger as the temperature is lowered and saturate at ∼100 K, confirming the presence of charge-ordering in the LTM (AFM-CE) phase. Thus we observed complete correspondence between the three distinct crystallographic phases revealed by the high-resolution X-ray

Table 6. Mn−O Bond Distances and Mn−O−Mn Bond Angles at 300 and 160 K

	sample 1			sample 2	
	T = 300 K	T = 160 K	T = 160 K	T = 300 K	T = 160 K
phase	HTO	HTO	LTO	HTO	HTO
Mn−O(eq) (Å)	4 × 1.9378(3)	4 × 1.9355(4)	1.9459(7)	4 × 1.9391(4)	4 × 1.9339(5)
Mn−O(ax) (Å)	2 × 1.9307(5)	2 × 1.9360(9)	1.894(2)	2 × 1.9310(7)	2 × 1.9291(7)
Mn−O(eq)−Mn (deg)	168.1(2)	167.9(2)	168.1(4)	167.83(23)	169.13(30)
Mn−O(ax)−Mn (deg)	162.2(2)	160.3(3)	168.0(4)	162.44(28)	162.94(28)

Table 7. Mn−O Bond Distances and Mn−O−Mn Bond Angles for Sample 2 at 50 K in the Charge-Ordered State

bond distances (Å)		bond angles (deg)	
Mn(3)[a]−O(3)	2 × 1.94(1)	O(3)−Mn(3A)−O(4)	92.71(5)
Mn(3)−O(4)	2 × 2.07(1)	O(3)−Mn(3A)−O(7)	91.5(6)
Mn(3)−O(7)	2 × 1.896(3)	O(4)−Mn(3A)−O(7)	90.7(6)
Mn(4)−O(ax)[b]	2 × 1.92(4)	O(eq)−Mn(4)−O(ax)	91.5(6)
Mn(4)−O(eq)[b]	4 × 1.90(2)	Mn(4)−O(ax)−Mn(4)	157.0(2)
		Mn(3)−O(ax)−Mn(3)	165.6(1)
		Mn(3)−O(eq)−Mn(4)	166.8(2)

[a] Due to the constraints used in the refinement the bond distances and angles around Mn(3B) are identical to those around Mn(3A). [b] Due to the use of a breathing rigid body to model the oxygens surrounding Mn(4) and O(1) through O(4) all have the same Mn−O distances and angles, as do O(5) and O(6). These are denoted O(eq) and O(ax), respectively.

Table 8. Values of the Magnetic Moment on the Manganese Ion (in Bohr magnetons), as Refined from the Neutron Diffraction Data Collected on Sample 1

	250 K	200 K	160 K	100 K	15 K
			HTO Phase[a]		
μ_y	0.48(4)	0.56(4)	0.56(6)	1.14(8)	1.1(2)
μ_z	−0.36(8)	1.91(4)	2.40(5)	3.2(1)	3.7(2)
μ_{tot}	0.60(6)	1.99(4)	2.47(5)	3.4(1)	3.9(3)
			LTO Phase[b]		
μ_x		1.89(1)	2.19(6)	3.66(6)	3.90(7)
			LTM Phase[c]		
Mn^{3+} μ_z				1.47(4)	1.79(4)
Mn^{4+} μ_z				1.35(3)	1.53(4)

[a] Magnetic space group = $Im'm'a$. [b] Magnetic space group = I_pmma. [c] Magnetic space group = $P_{2c}2_1/m$.

data, and the three magnetic structures identified from the neutron data. The conclusions regarding magnetic, orbital, and charge ordering are consistent with the structures determined from Rietveld refinements (Tables 3, 4, and 6). We note that the presence of both ferromagnetic and antiferromagnetic reflections is often interpreted in terms of a canted magnetic structure, but it is quite clear that this is not the case in the present material.

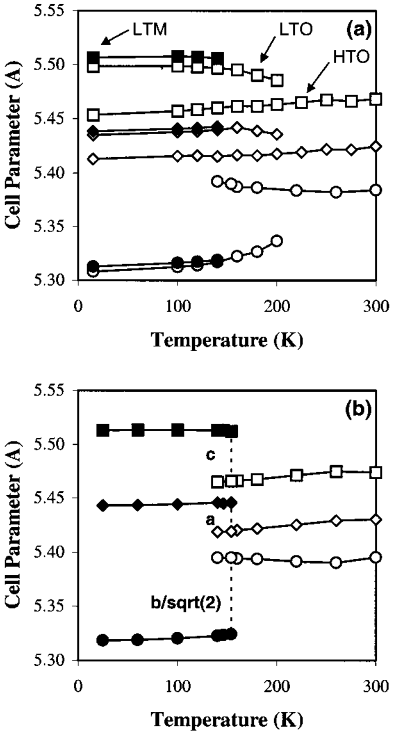

Figure 4. The temperature evolution of the unit cell parameters for each of the phases observed in (a) sample 1 and (b) sample 2. Diamonds, circles, and squares represent the a, $b/\sqrt{2}$, and c lattice parameters, respectively. The HTO and LTO phases are represented by open symbols, while the data points for the LTM phase are filled. All data was collected upon cooling with the exception of the points at 154 and 160 K in part b. Lines are shown only as guides to the eye.

The temperature dependence of the unit cell volume for each phase is shown in Figure 6. At 100 K and below, the volume of the HTO (FM) phase is systematically larger than the weighted average volume, which is essentially the same as that of the dominant charge-ordered LTM (AFM-CE) phase. On the other hand, the cell volume of the LTO (AFM-A) phase is significantly smaller than the average volume. Since the ionic radius of Mn^{4+} is smaller than that of Mn^{3+}, increasing the Mn^{4+} content is reflected in a decrease in the unit cell volume. This trend is observed for $Nd_{1-x}Sr_xMnO_3$ between $x = 0.50$ and 0.54,[29] even though the ionic radius of Sr is considerably larger than that of Nd. We therefore infer that the HTO phase is electron-rich (Mn^{4+}:Mn^{3+} < 1) and the LTO phase is electron-poor (Mn^{4+}:Mn^{3+} > 1). Such a conclusion is consistent with the magnetic phase diagram reported by Moritomo et al.[29] It is interesting to note that neutron powder data reported in that work for $Nd_{0.48}Sr_{0.52}MnO_3$ showed magnetic peaks characteristic of both AFM-A and AFM-CE structures at 10 K. The coexistence of two phases at that composition suggests that the AFM-CE phase is only stable within the approximate range $0.49 < x < 0.52$.

From the evolution of the phase fractions (Figure 7), we infer that ~25% of the HTO (FM) phase transforms to the LTO (AFM-A) phase in the temperature range 220−160 K, and that once the latter forms, it does not transform to the LTM (AFM-CE) phase. Most of the remaining HTO phase then transforms to the LTM phase between 150 and 100 K, but about 15% of the HTO phase is still present at 15 K. We once again note that these transformations are not accompanied by any measurable broadening of the diffraction peaks. The behavior of sample 1 is clearly markedly different from that reported for $Nd_{0.5}Sr_{0.5}MnO_3$ by Kuwuhara et al.[20] and Kawano et al.,[22] using crystals grown by the floating-zone method, in which a sharp transition from the FM to the AFM-CE phase was observed at ~160 K, with no evidence of the AFM-A phase.

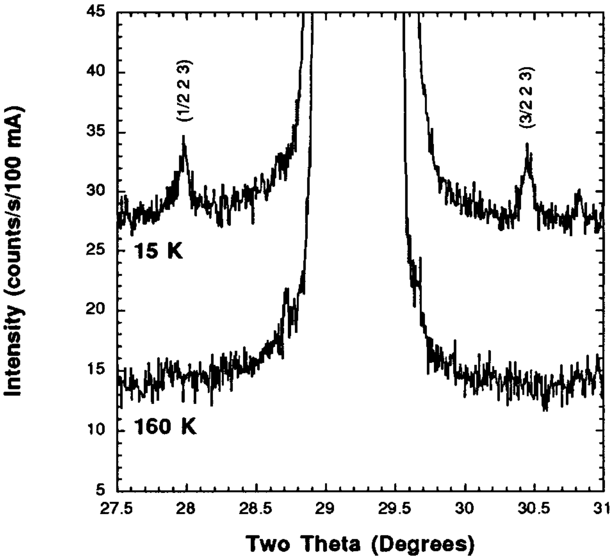

Figure 5. Highlighted regions of the X-ray diffraction patterns for sample 1, showing superstructure reflections confirming the presence of charge ordering in the LTM phase, but not the LTO phase.

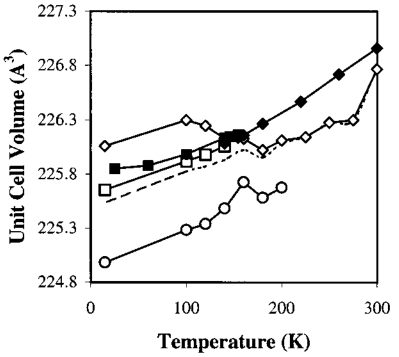

Figure 6. The temperature evolution of the unit cell volume. Diamonds, circles, and squares represent the HTO, LTO, and LTM phases, respectively. Open symbols are used for sample 1 and filled symbols for sample 2. The dotted line represents the average volume of sample 1. The average was obtained by weighting the volume of each phase by its phase fraction.

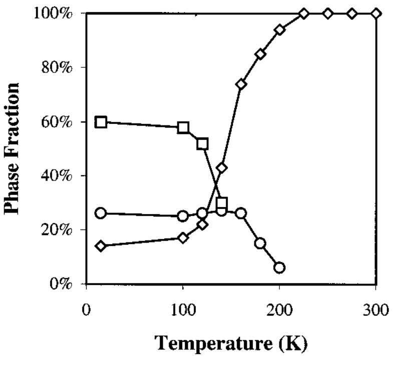

Figure 7. The temperature evolution of the phase fraction for sample 1. Diamonds, circles, and squares represent the HTO, LTO, and LTM phases, respectively.

Sample 2—Diffraction Results. Comparing the behavior of sample 1 with that of the earlier work done on single-crystal samples raises some interesting questions. Are these differences a consequence of small differences in the stoichiometry, as implied but certainly not proven by our compositional analysis, or do they reflect a fundamental difference between polycrystalline and single-crystal samples? In an attempt to answer this question a second sample was prepared, this time using MnO as a starting reagent in place of Mn_3O_4. Manganese(II) oxide was chosen as a starting reagent because its stoichiometry is generally more reliable than that of Mn_3O_4, reducing the probability that deviations from the ideal (metal) stoichiometry will be present in the final product.

High-resolution synchrotron X-ray data collected at room temperature, using the crystal-analyzer geometry (λ = 0.79935 Å), showed an orthorhombic phase with *Imma* symmetry as before, and lattice parameters a = 5.4312(3), b = 7.6321(4), c = 5.4754(3) Å. Data were also collected from sample 1 under the same conditions and are listed for comparison in Table 2. It should be noted that the cell volume of sample 2 is larger than that of sample 1 by a statistically significant amount, as would be expected if sample 2 is stoichiometric and sample 1 contains a slight excess of Mn^{4+}. Furthermore, the sample 2 diffraction peaks were noticeably sharper (~0.01–0.025° vs 0.015–0.045°), and from the Williamson–Hall analysis discussed above, we conclude that the fluctuations in the Nd:Sr ratio are noticeably smaller (±0.005 vs ±0.01).

Scans were made over selected peaks at several temperatures as before, and the resulting lattice parameters are similar to those which have previously been reported by Kuwuhara et al.[20] (see Figure 4). The only difference from the previous work is the existence of a two-phase coexistence region, observed at 140 K on cooling and 154 K on heating, indicative of a significant hysteresis effect.[42] In this coexistence region, the diffraction peaks for both phases are still extremely sharp, suggesting that individual crystallites transform without breaking up into domains. Furthermore, although the lattice parameters of the coexisting phases are substantially different as a result of orbital ordering in the low-temperature LTM phase, their unit cell volumes are the same within 0.02%, 225.996(6) Å^3 and 226.03(1) Å^3 for the FM phase and AFM-CE phase respectively at 154 K, and there is only a slight indication of a volume discontinuity within this temperature range (see Figure 6). No additional peaks corresponding to the AFM-A phase were seen in any of the scans.

Extended X-ray data sets suitable for Rietveld refinement were collected from a capillary sample at 300, 160 and 50 K using the linear PSD detector and a wavelength of 0.8017 Å. Refinement of the A-site cation occupancies did not indicate any departure from stoichiometry in this sample. Refinements of the HTO phase at 300 K in the paramagnetic state and at 160 K in the ferromagnetic state are detailed in Tables 3 and 5. Bond distances, angles are reported in Table 6. The structures of the HTO phase in sample 2 seem to be very similar to those found for sample 1 at the same temperatures.

Refinement of the Charge-Ordered Structure. Superlattice peaks characteristic of the charge-ordered LTM phase are clearly visible at 50 K (see Figure 8),

---

(42) A small amount of the sample (~3%) did not transform from the HTO phase to the charge-ordered structure even down to 50 K. However, this type of behavior is not unusual for low temperature first-order phase transitions.

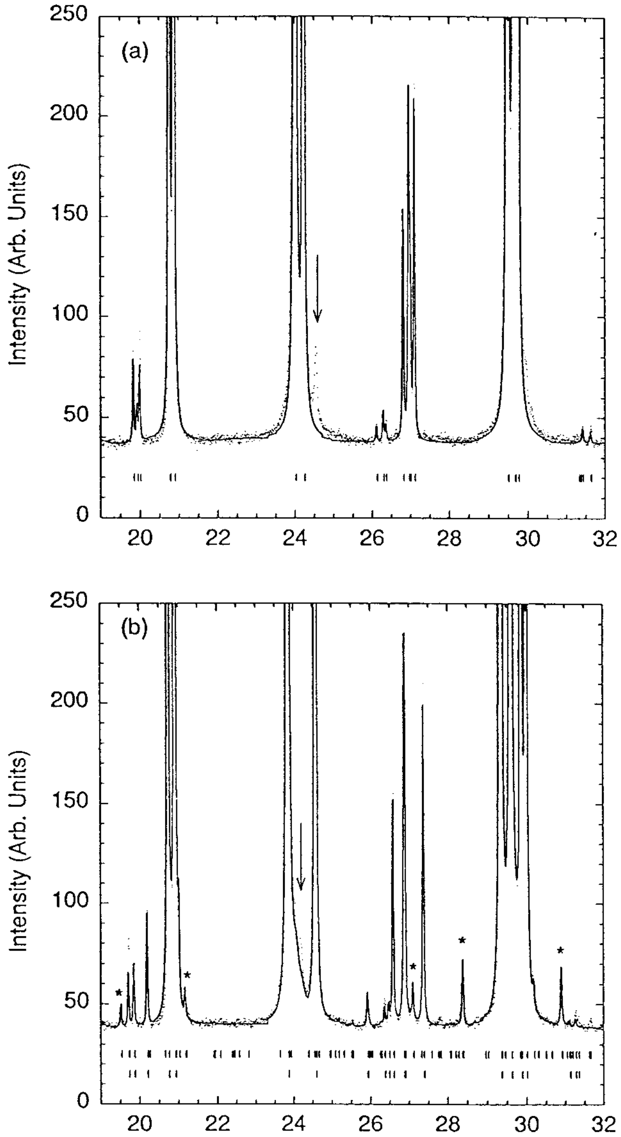

Figure 8. Portions of the X-ray diffraction pattern taken on sample 2 at (a) 160 K and (b) 50 K. The vertical scale has been greatly expanded to show the superstructure reflections clearly. The observed intensities are plotted as dots, while the Rietveld fit is plotted as a solid line. The tick marks beneath the plot mark the calculated peak positions. Peaks marked with asterisks represent superstructure reflections, which arise due to charge ordering. The peak marked with an arrow in part a originates from the incipient charge-ordered phase, while the peak marked with an arrow in part b originates from the residual high-temperature phase.

and these peaks appear to be somewhat stronger and sharper than the charge-ordering peaks observed in the low-temperature diffraction patterns of sample 1. Despite the large body of research devoted to the study of the manganate perovskites, there are very few crystal structure determinations of these materials in the charge-ordered state. The high-quality data obtained from sample 2 at 50 K permits refinement of the charge-ordered structure for $Nd_{0.5}Sr_{0.5}MnO_3$. However, due to the high degree of pseudo-symmetry present in the structure it is necessary to impose some constraints in the refinement.

Refinements of the charge-ordered structure of $La_{0.5}Ca_{0.5}MnO_3$ show that there are two distortion mechanisms characteristic of the charge-ordered structure.[9] The first is a contraction of the Mn−O(eq) bonds about the tetravalent manganese ions. The second is a cooperative shift of the Mn^{4+}-centered octahedra in the *z* direction to facilitate spatial ordering of the filled e_g orbitals on Mn^{3+}. To combine these degrees of freedom with those present due to octahedral tilting the following constraints were employed. A planar $Mn(4)O(eq)_4$ rigid body was defined so that all Mn(4)−O(eq) [O(eq) = O(1), O(2), O(3), O(4)] distances become equivalent and all O(eq)−Mn(4)−O(eq) angles are 90°. The rigid body was then allowed to translate in the *z* direction, rotate about an axis parallel to *a*,[43] and breathe (the Mn(4)−O(eq) distance was refined). The Sr/Nd cations were allowed to translate only in the *z* direction and the displacements of Sr/Nd(1) and Sr/Nd(2) as well as Sr/Nd(3) and Sr/Nd(4) were constrained to be equal in magnitude, but opposite in direction (consistent with the displacement of the Mn(4) centered octahedra as dictated by the space group symmetry). The positions of the axial oxygens [O(5)−O(8)] were allowed to translate in the *z* direction only. Finally, O(5) and O(6) were related to each other by an inversion center on Mn(4). This is similar to the constrained model Radaelli et al. used to refine $La_{0.5}Ca_{0.5}MnO_3$,[9] but the $Mn(4)O(eq)_4$ breathing and rotation modes represent additional degrees of freedom in this model. Refinements using this constrained model gave very good fits to the observed diffraction pattern. The Mn(4)-centered octahedra were found to shift by 0.09 Å and the Sr/Nd(1):Sr/Nd(2) ions by 0.07 Å. A 9.4(2)° rotation of the $Mn(4)O_6$ octahedra about *a* was observed, and Mn(4)−O(eq) distance was refined to 1.90(2) Å. The Sr/Nd(3):Sr/Nd(4) ions did not shift from their ideal sites. Results of the refinement and bond valences are contained in Tables 3 and 5, while selected bond distances and angles are listed in Table 7. The bond distances clearly show the presence of charge and orbital ordering. The bond valences for the A-site and oxygen ions are also reasonable. A section of the charge-ordered structure is shown in Figure 9. We note that the charge-ordered structures of $La_{0.5}Ca_{0.5}MnO_3$ and $Nd_{0.5}Sr_{0.5}MnO_3$ are very similar, the primary difference can be attributed to different octahedral tilting distortions ($a^-b^+a^-$ for $La_{0.5}Ca_{0.5}MnO_3$ and $a^-b^0a^-$ for $Nd_{0.5}Sr_{0.5}MnO_3$).

Several attempts were made to loosen the constraints used in the refinement. When the constraints on the Nd/Sr positions were removed, these ions tended to stay very close their constrained positions. When the constraints on the oxygen position were lifted, the oxygen positions drifted off so that the Mn−O and Sr/Nd−O bond distances became less reasonable. In no instance was the fit to the experimental diffraction pattern improved by loosening of the constraints.

Discussion

The dramatically different phase-transition behavior exhibited by samples 1 and 2 is certainly unexpected, in light of the fact that both samples would appear to have similar compositions, and would certainly be regarded as highly homogeneous by normal X-ray

---

(43) This corresponds to the octahedral rotation present in the $a^-b^0a^-$ tilt system (space group *Imma*) characteristic of the room-temperature structure.

(44) Brown, I. D. *J. Appl. Crystallogr.* **1996**, *29*, 479.

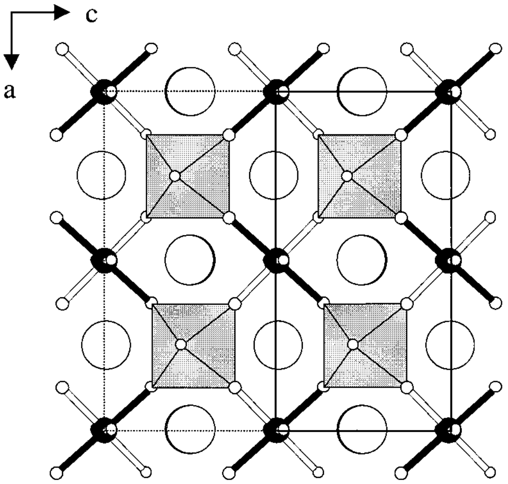

Figure 9. A (010) layer of the charge-ordered structure, as refined for $Nd_{0.5}Sr_{0.5}MnO_3$ (sample 2) from X-ray diffraction data at 50 K. The Mn^{4+}-centered octahedra are represented in polyhedral notation, the Mn^{3+} ions as filled spheres, the Nd/Sr cations as large open spheres, while the oxygens are depicted as small open spheres. The long $Mn^{3+}-O$ bonds are shown in black, and represent the orientation of occupied e_g orbitals. The unit cell in the *ac* plane is depicted by the solid line. The *c* axis of the magnetic unit cell is doubled with respect to the *c* axis of the crystal structure, as depicted by the dotted line.

standards. The coexistence of three macroscopically distinct crystallographic and magnetic phases over a wide temperature range in the first, but not the second sample, must originate from either the slightly higher Mn^{4+} content, and/or the larger compositional fluctuations (inferred from the X-ray peak widths) of the first sample. The small compositional variations between crystallites appear to be effectively masked at room temperature, because of the isotropically delocalized nature of the e_g electrons, which do not couple with the lattice as they do at low temperatures in the orbital- and charge-ordered phases. One very simple picture is to imagine each crystallite having lattice parameters and stoichiometry defined by its Mn^{4+} content, which determines whether the FM (HTO) phase transforms to the orbitally ordered AFM-A structure (LTO), to the charge-ordered AFM-CE structure (LTM), or not at all. If there is a Gaussian distribution of such crystallites, the results can be interpreted on the basis of the electronic phase diagram for $Nd_{1-x}Sr_xMnO_3$ depicted in ref 29. The transformations in the first sample would then correspond roughly as follows: FM to AFM-A between 225 and 160 K for $Mn^{4+} > 0.52$, FM to AFM-CE between 160 and 110K for Mn^{4+} between 0.49 and 0.52, and no transformation (other than PM to FM) for $Mn^{4+} < 0.49$. This is qualitatively consistent with the range in compositional fluctuations (fwhm implies $x \sim 0.02$) inferred from the X-ray peak widths, the slight excess of Mn^{4+}, and the unit cell volumes below 100 K. On the other hand, our observation that the second sample transforms completely from FM to AFM-CE over a relatively narrow temperature range (probably a couple of degrees Kelvin, although we have not investigated this in detail), reflects the smaller compositional fluctuations (fwhm implies $x \sim 0.01$) and average Mn^{4+} content very near to the ideal 1:1 Mn^{4+}:Mn^{3+} ratio, associated with this sample.

Conclusions

The results reported in this paper dramatically demonstrate the intense competition between the ferromagnetic metallic state, the antiferromagnetic A-type state, and the charge-ordered, antiferromagnetic CE-type state in the $Nd_{1-x}Sr_xMnO_3$ phase diagram, near $x = 0.5$. The Coulomb stabilization associated with long-range charge and orbital ordering of Mn^{3+}/Mn^{4+} is absolutely essential to stabilize the AFM-CE state, with respect to the competing delocalized e_g electron states. Very small changes in the Mn^{4+}:Mn^{3+} ratio stabilize the FM state when the $Mn^{4+}:Mn^{3+} < 1$, and stabilize the AFM-A state when the $Mn^{4+}:Mn^{3+} > 1$. The structure of the charge-ordered AFM-CE state has been determined and found to be very similar to charge-ordered state previously observed for $La_{0.5}Ca_{0.5}MnO_3$.[9] The charge-ordered state appears to be stable only over a very narrow compositional range.

Finally, we conclude that the standard powder diffraction techniques commonly used as the criterion for “single-phase material” are not an adequate indicator of sample quality for these manganate systems; in particular, the possible coexistence of crystallographically distinct phases should be carefully considered in the interpretation of all measurements on these compounds, and particularly in the context of coexisting vs canted magnetic structures.

Acknowledgment. This work was partially supported by the U.S. Department of Energy under contract #DE-AC02-98CH10886. We acknowledge the NIST Center for Neutron Research for access to and Brian Toby for assistance in the use of the BT1 neutron powder diffractometer. Finally, we thank Pavel Karen, of the University of Oslo, for performing the iodometric titrations and Anthony Arulraj of the Indian Institute of Science for preparation of sample 1.

CM990281D